New Journal of Physics
The open-access journal for physics

Turbulence in collisionless plasmas: statistical analysis from numerical simulations with pressure anisotropy

G Kowal[1,2,3,5], D A Falceta-Gonçalves[3,4] and A Lazarian[3]

[1] Instituto de Astronomia, Geofísica e Ciências Atmosféricas, Universidade de São Paulo, Rua do Matão 1226, 05508-900, São Paulo, Brazil
[2] Obserwatorium Astronomiczne, Uniwersytet Jagielloński, Orla 171, 30-244 Kraków, Poland
[3] Department of Astronomy, University of Wisconsin, 475 North Charter Street, Madison, WI 53706, USA
[4] Escola de Artes, Ciências e Humanidades, Universidade de São Paulo, Rua Arlindo Bettio 1000, CEP 03828-000, São Paulo, Brazil
E-mail: kowal@astro.iag.usp.br

New Journal of Physics **13** (2011) 053001 (23pp)
Received 22 December 2010
Published 3 May 2011
Online at http://www.njp.org/
doi:10.1088/1367-2630/13/5/053001

Abstract. In recent years, we have experienced increasing interest in the understanding of the physical properties of collisionless plasmas, mostly because of the large number of astrophysical environments (e.g. the intracluster medium (ICM)) containing magnetic fields that are strong enough to be coupled with the ionized gas and characterized by densities sufficiently low to prevent the pressure isotropization with respect to the magnetic line direction. Under these conditions, a new class of kinetic instabilities arises, such as firehose and mirror instabilities, which have been studied extensively in the literature. Their role in the turbulence evolution and cascade process in the presence of pressure anisotropy, however, is still unclear. In this work, we present the first statistical analysis of turbulence in collisionless plasmas using three-dimensional numerical simulations and solving double-isothermal magnetohydrodynamic equations with the Chew–Goldberger–Low laws closure (CGL-MHD). We study models with different initial conditions to account for the firehose and mirror instabilities and to obtain different turbulent regimes. We found that the CGL-MHD subsonic and supersonic turbulences show small differences compared

[5] Author to whom any correspondence should be addressed.

to the MHD models in most cases. However, in the regimes of strong kinetic instabilities, the statistics, i.e. the probability distribution functions (PDFs) of density and velocity, are very different. In subsonic models, the instabilities cause an increase in the dispersion of density, while the dispersion of velocity is increased by a large factor in some cases. Moreover, the spectra of density and velocity show increased power at small scales explained by the high growth rate of the instabilities. Finally, we calculated the structure functions of velocity and density fluctuations in the local reference frame defined by the direction of magnetic lines. The results indicate that in some cases the instabilities significantly increase the anisotropy of fluctuations. These results, even though preliminary and restricted to very specific conditions, show that the physical properties of turbulence in collisionless plasmas, as those found in the ICM, may be very different from what has been largely believed. Implications can range from interchange of energies to cosmic ray acceleration.

Contents

1. Introduction

Magnetized and low-density (weakly collisional) plasmas are known to present anisotropic pressures with respect to the magnetic field orientation, which can survive for considerably long periods compared with the dynamical timescales of certain systems. In astrophysical environments, such pressure anisotropy may be generated by several different processes, such as kinetic pressure of cosmic rays, supernovae explosions, stellar winds or anisotropic turbulent motions (see Quest and Shapiro 1996).

Under certain conditions, gyrotropic plasmas give rise to new wave modes and instabilities, which cannot be studied by the standard isotropic magnetohydrodynamic (MHD) model (Hasegawa 1969, Wang and Hau 2003, Passot and Sulem 2006). For instance, Hau and Wang (2007) showed that gyrotropic MHD equations closed by the Chew–Goldberger–Low laws (CGL-MHD) lead to a positive density n versus magnetic field strength B correlations for the slow magnetosonic mode under certain conditions in contradiction to the standard MHD model. It was commonly believed that the detected absence of slow modes in several astrophysical sites is related to the strong damping of these waves. However, in the collisionless plasmas, it could be explained by wrong identification of the positive n–B correlations for fast magnetosonic modes.

The pressure anisotropies give rise to plasma instabilities depending on the anisotropy ratio, e.g. $p_\parallel > p_\perp$ and $p_\perp > p_\parallel$ for the firehose and mirror instabilities, respectively. They are responsible for the growth of the magnetic energy and acceleration of particles. The predictions of the CGL-MHD model, including new plasma instabilities, are also important in weakly magnetized environments, since even a weak magnetic field is enough to change the motion of the charged particles and therefore increase the pressure anisotropy.

As an example of the possible applications, Sharma *et al* (2003) and Sharma *et al* (2006) showed the importance of the collisionless plasma approach in protostellar discs. They studied the role of the kinetic instabilities in the magneto-rotational instability (MRI) showing that the transport of angular momentum in the disc may be efficiently increased under certain circumstances.

The intracluster medium (ICM) is possibly the most suitable environment for studies of gyrotropic plasma effects (Schekochihin *et al* 2005). Considering typical parameters of $n \sim 10^{-3}\,\mathrm{cm}^{-3}$, $T \sim 10^7\,\mathrm{K}$ and $B \sim 1\,\mu\mathrm{G}$ (Ensslin and Vogt 2006), it is possible to show that the cyclotron frequency (Ω) is much larger than the collision frequency (ν_{ii}). Under such conditions, the plasma fluctuations with wave numbers $k \geqslant 1\,\mathrm{kpc}$ will be subject to different processes related to the pressure anisotropy. The turbulent cascade, for example, may be modified by the new wave modes and instabilities, resulting in a different picture of the energy budget in these environments. It may be particularly important for the understanding of the cooling flow and the cosmic rays acceleration processes.

Schekochihin *et al* (2008) showed that in the ICM, the anisotropy-induced firehose and mirror instabilities may grow nonlinearly up to saturation at $\delta B/B \sim 1$. This growth is very fast. They estimated the increase in power at small scales. As a consequence, the excess of small-scale fluctuations of B and the energy transport at these environments may drastically change the picture. In certain cases, the small scales may also be considered as collisionless, which may be important, for instance, for the development of the turbulent cascade. For wavelengths smaller than the Larmor radius, kinetic treatment of plasma is necessary, as shown by Howes *et al* (2006). However, in this work we focus on the large scale; hence the CGL-MHD approximation may be used instead.

The aim of this work is to provide an extensive statistical analysis of the MHD turbulence in collisionless plasmas and to study the role of different instabilities in the evolution of the system. To accomplish that, we performed the first three-dimensional (3D) simulations focusing on the evolution of turbulence in the presence of pressure anisotropy. A description of the model as well as the presentation of the governing equations is given in section 2, with an additional discussion of the instabilities and double-isothermal approximation. In section 3, we describe the numerical simulations. The results and an extensive statistical analysis including

the derivation of probability distribution functions (PDFs), spectra and structure functions of the fluctuations in density and velocity are presented in section 4. We discuss the most important results in section 5 and present in section 6 the main conclusions drawn.

2. The double-isothermal Chew–Goldberger–Low magnetohydrodynamical (CGL-MHD) approximation

2.1. Governing equations

In the fluid approximation, a gyrotropic plasma can be described by the Chew *et al* (1956) magnetohydrodynamic (called CGL-MHD henceforth) equations expressed in conservative form as follows,

$$\frac{\partial \rho}{\partial t} + \nabla \cdot (\rho \boldsymbol{v}) = 0, \tag{1a}$$

$$\frac{\partial \rho \boldsymbol{v}}{\partial t} + \nabla \cdot \left[\rho \boldsymbol{v}\boldsymbol{v} + \left(\mathsf{P} + \frac{B^2}{8\pi} \right) I - \frac{1}{4\pi} \boldsymbol{B}\boldsymbol{B} \right] = \boldsymbol{f}, \tag{1b}$$

$$\frac{\partial \boldsymbol{B}}{\partial t} - \nabla \times (\boldsymbol{v} \times \boldsymbol{B}) = 0, \tag{1c}$$

where ρ and $\boldsymbol{v}$ are the plasma density and velocity, respectively, $\boldsymbol{B}$ is the magnetic field, $\mathsf{P} = p_\perp \hat{I} + (p_\parallel - p_\perp)\hat{b}\hat{b}$ is the pressure tensor, $\hat{b} = \mathbf{B}/|\mathbf{B}|$ is the unit vector along the magnetic field, $p_\parallel$ and $p_\perp$ are the pressure components parallel and perpendicular to $\hat{b}$, respectively, and $\boldsymbol{f}$ represents the forcing term.

The above set of equations will be complete with the description of the parallel and perpendicular pressure components. To avoid the complexities related to explicitly calculated processes that may be important for the description of the energies, e.g. the anisotropic heat conduction and the emission and absorption of the radiation, we can make use of the double-polytropic equations instead, as suggested by Chew *et al* (1956). Tests of this approximation using the solar magnetosheath data confirmed its validity under the form (see Hau and Sonnerup 1993)

$$\frac{\mathrm{d}}{\mathrm{d}t} \left(\frac{p_\perp}{\rho B^{\gamma_\perp - 1}} \right) = 0, \tag{2a}$$

$$\frac{\mathrm{d}}{\mathrm{d}t} \left(\frac{p_\parallel B^{\gamma_\parallel - 1}}{\rho^{\gamma_\parallel}} \right) = 0, \tag{2b}$$

where $\gamma_\perp$ and $\gamma_\parallel$ are the polytropic exponents for the perpendicular and parallel pressures, respectively. These equations, according to Hau (2002), can be expressed in the conservative form, as

$$\frac{\partial S_\perp}{\partial t} + \nabla \cdot (S_\perp \boldsymbol{v}) = 0, \tag{3a}$$

$$\frac{\partial S_\parallel}{\partial t} + \nabla \cdot \left(S_\parallel \boldsymbol{v} \right) = 0, \tag{3b}$$

where $S_\perp = p_\perp B^{1-\gamma_\perp}$, $S_\parallel = p_\parallel (B/\rho)^{\gamma_\parallel - 1}$ and $B = |\boldsymbol{B}|$ is the strength of the magnetic field. In this form, the double-polytropic equations can be solved numerically, similar to the continuity equation.

2.2. Double-isothermal closure

Under the double-isothermal closure, we have $\gamma_{\parallel} = \gamma_{\perp} = 1$ and the equation of state is described by two relations, $p_{\perp} = a_{\perp}^2 \rho$ and $p_{\parallel} = a_{\parallel}^2 \rho$, where $a_{\perp}$ and $a_{\parallel}$ are constants and represent speeds of sound along the perpendicular and parallel directions to the magnetic field, respectively. In such a situation, the conservative form of the momentum equation for the double-isothermal CGL-MHD model can be rewritten as

$$\frac{\partial \rho \mathbf{v}}{\partial t} + \nabla \cdot \left[\left(a_{\perp}^2 \rho + \frac{B^2}{8\pi} \right) \hat{I} - (1-\alpha)\, \mathbf{BB} \right] = \boldsymbol{f}, \tag{4}$$

where $\alpha \equiv \frac{1}{2}(\beta_{\parallel} - \beta_{\perp}) \equiv \frac{1}{2}\beta_{\perp}\,(\xi - 1)$, $\xi \equiv p_{\parallel}/p_{\perp}$ is the pressure anisotropy ratio, and $\beta_{\parallel} \equiv p_{\parallel}/p_{\mathrm{mag}}$ and $\beta_{\perp} \equiv p_{\perp}/p_{\mathrm{mag}}$ are the plasma betas in the parallel and perpendicular directions to the local field, respectively.

The main consequence of the double-isothermal closure is that the pressure anisotropy is kept constant, i.e. $\xi = \mathrm{const}$, independent of the evolution of the kinetic instabilities that may arise. Therefore, the stability condition is fulfilled by the local decrease in density and the increase in magnetic pressure, and is not due to the local changes in the pressure tensor.

Furthermore, this work is focused on the study of the differences between the turbulent regimes in collisionless plasmas and standard MHD turbulence using as reference the studies performed by Kowal *et al* (2007) and Kowal and Lazarian (2010), where an extensive statistical analysis of density, velocity and magnetic field distributions in the isothermal MHD simulations is presented. For this reason, we chose the double-isothermal CGL-MHD model as a natural extension of the isothermal MHD in order to understand the importance of pressure anisotropy and its consequences on the turbulent plasmas.

2.3. Firehose and mirror instabilities

While in the MHD model the dispersion relations do not exhibit any instabilities, in the CGL-MHD equations the term of the pressure anisotropy introduces significant changes to the dynamical system. The detailed linearization and wave analysis of the double-isothermal CGL-MHD equations is provided in the appendix. Here, we describe the final dispersion formulae resulting from the presence of pressure anisotropy. For example, in the case of the incompressible Alfvén mode, the dispersion relation can be written as

$$\left(\omega^2/k^2\right)_A = c_A^2\,(1-\alpha)\cos^2\theta, \tag{5}$$

where $\alpha \equiv \frac{1}{2}(\beta_{\parallel} - \beta_{\perp})$ and θ is the angle between the mean field and the wave vector of the perturbation. Equation (5) becomes negative when $\beta_{\parallel} - \beta_{\perp} > 2$, which results in the occurrence of firehose instability and the growth of the magnetic field fluctuations. As a consequence, the field lines bend and the magnetic pressure increases, reducing the parameter α to its saturation value $\alpha \approx 2$. This is known as the kinetic Alfvén firehose instability. Two other instabilities related to the slow mode are called the compressible firehose and mirror instabilities and occur when $p_{\parallel} > p_{\perp}$ or $p_{\perp} > p_{\parallel}$, respectively, and the dispersion relation for magnetosonic waves becomes negative (see the appendix).

In figure 1, we show the stability regimes for two cases of the pressure anisotropy studied in this paper, $a_{\parallel}/a_{\perp} = 0.5$ in the left panel and $a_{\parallel}/a_{\perp} = 2.0$ in the right one (corresponding to $p_{\parallel}/p_{\perp} = 0.25$ and $p_{\parallel}/p_{\perp} = 4.0$, respectively), plotted as functions of the plasma beta $\beta_{\parallel}$ related to the parallel pressure and the squared sinus of the angle between the directions of

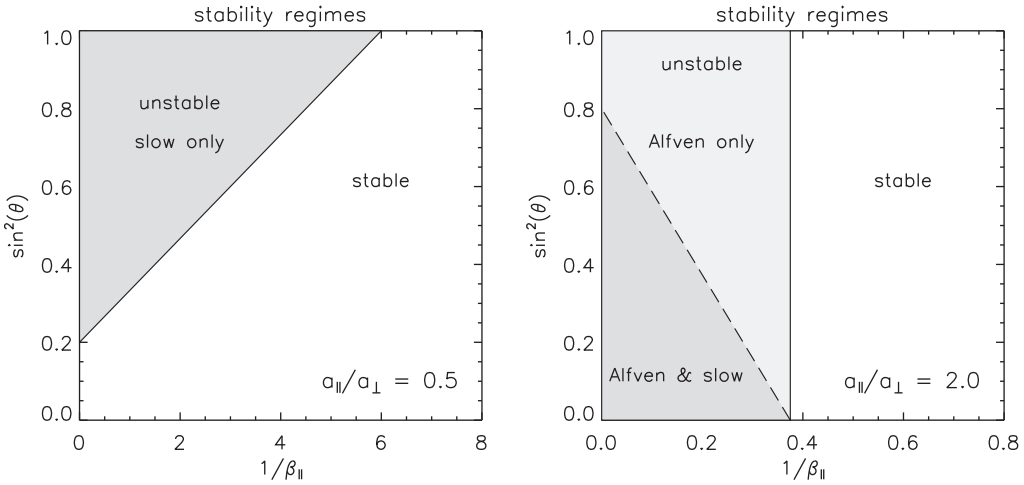

Figure 1. Stability conditions for models with the sound speed ratio $a_\parallel/a_\perp = 0.5$ (left panel) and $a_\parallel/a_\perp = 2.0$ (right panel). On the horizontal axis, we show the plasma beta parameter related to the parallel pressure and defined as $\beta_\parallel \equiv p_\parallel/p_{\rm mag} = 2a_\parallel^2/c_A^2$, where $p_{\rm mag} \equiv \frac{1}{2}|B|^2$ is the magnetic pressure. On the vertical axis, we show the squared sinus of the angle between the directions of the perturbation and the mean field.

the perturbation propagation and magnetic field. When the perpendicular pressure dominates (left panel), only the mirror instability corresponding to the slow mode can occur. When perturbations propagate in directions almost perpendicular to the magnetic field, the range of unstable $\beta_\parallel$ grows. In contrast, when the direction of propagation is close to the direction of magnetic field, instability does not occur. In the case of dominating parallel pressure (right panel), the plasma becomes unstable due to two firehose instabilities related to the incompressible Alfvén and compressible slow modes, but the Alfvén mode firehose instability extends over a larger region of the parameter space up to $\beta_\parallel = 0.375$ independent of the angle between the perturbation propagation and magnetic field directions.

Both instabilities have the growth rate $\gamma \equiv \mathrm{Im}(\omega)$ larger at smaller scales, i.e. increasing with the wave number k. This dependence introduces a stiffness in the numerical integration since the micro-instabilities, which may be due to the numerical imprecision, tend to grow very fast and destroy the configuration of the studied problem. As a consequence, the pressure anisotropy tends to disappear quickly and the problem of interest cannot be studied. Sharma *et al* (2006) who studied the MRI in protostellar discs pointed out this important problem. They bypassed it by implementing a quasi-stability condition for the computational cells where the pressure anisotropy was larger than the threshold for instability. Physically, it can be understood as an almost 'instantaneous' evolution of the system to the quasi-stable condition. Under such conditions, all anisotropic effects are kept at the large scales and the problem of interest could be analyzed. The downside of this method is that it artificially removes the free energy of pressure anisotropy without, as a counterpart, increasing the kinetic and/or magnetic energies. That is because, in the physical sense, the instability increases the magnetic energy and/or accelerates the gas.

In the case of turbulence, this kind of artificial removal of the energy at small scales may not be the best approach because the small-scale structures in turbulence are generated by the

cascade process operating in the turbulent models, and therefore by artificially influencing the dissipation of energy we can distort its physical meaning and obtain incorrect conclusions. Nevertheless, under the double-isothermal approximation, the pressure anisotropy is kept even after the growth of the small-scale perturbations saturates, so the stability condition at large scales may lie in the unstable region even after saturation at small scales. Therefore, under certain conditions, the double-isothermal approximation is valid and might be an interesting area for studies of the evolution of turbulence in a collisionless plasma.

3. Numerical simulations

The simulations of turbulence in collisionless plasma were performed solving the set of double-isothermal CGL-MHD equations in a conservative form given by equations (1*a*)–(1*c*) with an addition term $\boldsymbol{f}$ in the motion equation representing the turbulence driving. The numerical integration of the system evolution governed by the CGL-MHD equations were performed by using the second-order shock-capturing Godunov-scheme code (Kowal *et al* 2007, 2009, Kowal and Lazarian 2010). We incorporated the field interpolated constrained transport (CT) scheme (see e.g. Tóth 2000) into the integration of the induction equation to maintain the $\mathrm{div}\,\boldsymbol{B} = 0$ constraint numerically. The numerical fluxes for the update of the fluid variables are obtained by using the general Harten–Lax–van Leer Riemann solver (Einfeldt *et al* 1991). The time integration was done with the second-order Runge–Kutta method (see e.g. Press *et al* 1992). On the right-hand side, the source term $\boldsymbol{f}$ represents a random solenoidal large-scale driving force. The rms velocity δv is maintained to be approximately unity, so that $\boldsymbol{v}$ can be viewed as the velocity measured in units of the rms velocity of the system and $\boldsymbol{B}/\sqrt{4\pi\rho}$ as the Alfvén velocity in the same units. The time t is in units of the large eddy turnover time ($\sim L/\delta v$) and the length in units of L, the scale of the energy injection. The magnetic field consists of the uniform background field and a fluctuating field: $\boldsymbol{B} = \boldsymbol{B}_0 + \boldsymbol{b}$. Initially, $\boldsymbol{b} = 0.0$. We use units in which the Alfvén speed $c_\mathrm{A} = B_0/\sqrt{4\pi\rho} = 1.0$ and $\rho = 1.0$ initially.

For our calculations, similar to our earlier studies (Kowal *et al* 2007, Kowal and Lazarian 2010), the sound speeds and the strength of the external field B_0 are the controlling parameters defining the sonic Mach number $\mathcal{M}_\mathrm{s} = \langle \delta v/a \rangle$ and the Alfvénic Mach number $\mathcal{M}_\mathrm{A} = \langle \delta v/c_\mathrm{A} \rangle$, respectively. The angle brackets $\langle\rangle$ signify averaging over the volume. $\mathcal{M}_\mathrm{s} < 1$ and $\mathcal{M}_\mathrm{s} > 1$ define subsonic and supersonic regimes, respectively, and $\mathcal{M}_\mathrm{A} < 1$ and $\mathcal{M}_\mathrm{A} > 1$ define two more regimes, sub-Alfvénic and super-Alfvénic, respectively. Since these two parameters are independent, we can analyze, for example, supersonic sub-Alfvénic turbulence, which signifies that $\mathcal{M}_\mathrm{s} > 1$ and $\mathcal{M}_\mathrm{A} < 1$. In the case of the CGL-MHD simulations, the regimes are defined by two sonic Mach numbers corresponding to the parallel and perpendicular sounds speeds.

We drove turbulence solenoidally at wave scale k equal to about 2.5 (2.5 times smaller than the size of the box). This scale defines the injection scale in our models. We did not set the viscosity and diffusion explicitly in our models. The scale at which the dissipation starts to act is defined by the numerical diffusivity of the scheme.

We performed six 3D CGL-MHD simulations using the resolution 512^3 for different initial conditions, as shown in table 1. We simulated the clouds up to $t_\mathrm{max} \sim 6$, i.e. 6 times longer than the dynamical timescale, to ensure full development of the turbulent cascade. The computational time required for each CGL-MHD simulation with intermediate resolution was equivalent to an MHD 512^3, as performed by Kowal *et al* (2007) and Kowal and Lazarian (2010).

Table 1. Description of the performed simulations of the double-isothermal CGL-MHD turbulence with the resolution 512^3. The initial density for all models was set to 1.0.

Model	B_0	$a_\parallel$	$a_\perp$	$\xi \equiv a_\parallel^2/a_\perp^2$	$\mathcal{M}_s \equiv \langle \lvert v \rvert / a_\perp \rangle$	$\mathcal{M}_A \equiv \langle \lvert v \rvert / c_A \rangle$
1	1.0	1.0	2.0	0.25	0.7	0.7
2	1.0	1.0	0.5	4.00	0.7	0.7
3	0.1	0.1	0.2	0.25	7.0	2.0
4	0.1	0.1	0.05	4.00	7.0	2.0
5	0.1	1.0	0.5	4.00	0.7	2.0
6	1.0	0.1	0.2	0.25	7.0	0.7

Models 1 and 2 are examples of weak turbulence and belong to subsonic and sub-Alfvénic regimes. The difference between these models is the pressure anisotropy accounting for the mirror and firehose instabilities. The comparison of both models gives us insights into the different evolutions of turbulence in the two cases. Similarly, we calculated models 3 and 4 for strong turbulence resulting in the supersonic and super-Alfvénic regimes. Again, we tested these regimes for different instabilities. Model 5 belongs to the subsonic and super-Alfvénic regimes representing the physical conditions of the ICM, and can be used as reference for further studies on this subject. Finally, model 6 belongs to the supersonic and sub-Alfvénic turbulent regimes and is the only simulation initiated with magnetic pressure larger than the thermal one. In this model, all cells are initially stable but as the turbulence develops unstable conditions can occur. In the following sections, we present the results obtained for each model, as well as a direct comparison with the standard MHD turbulent simulations with similar initial conditions.

4. Results

4.1. Distribution of density and velocity

The results obtained for the distribution of density and velocity show strong differences between the CGL-MHD and standard MHD models. However, the kinetic instabilities play a role in the evolution of turbulence under specific conditions. In figure 2, we present the column density obtained for each CGL-MHD model, as as well as the MHD models for comparison. Each case is presented as labeled in table 1, with the MHD case shown on the left and the CGL-MHD on the right.

From the column density maps it is possible to distinguish between models 2 and 5. Both models are subsonic, where initially we set $p_\parallel/p_\perp = 2$, which resulted in strong firehose instabilities. Here, the firehose instability is responsible for deformation of the magnetic field lines. The curved magnetic lines tend to slow down and trap the flowing gas. Since the growth rate is larger at small scales, we expect this effect to create more granulated maps. This is not seen in model 4 because $\rho\delta v^2 > p_\parallel \delta B^2$ and, therefore, the turbulence is able to destroy the configuration of the growing instability. The same occurs for model 3. Even though it is not visible in the column density maps, the kinetic instabilities are responsible for changes in the statistics of the turbulence, as addressed below. For models 1 and 6, in which $p_\parallel/p_\perp = 0.5$, the column density maps show mild differences. In these cases, we have a mirror instability

IOP Institute of Physics DEUTSCHE PHYSIKALISCHE GESELLSCHAFT

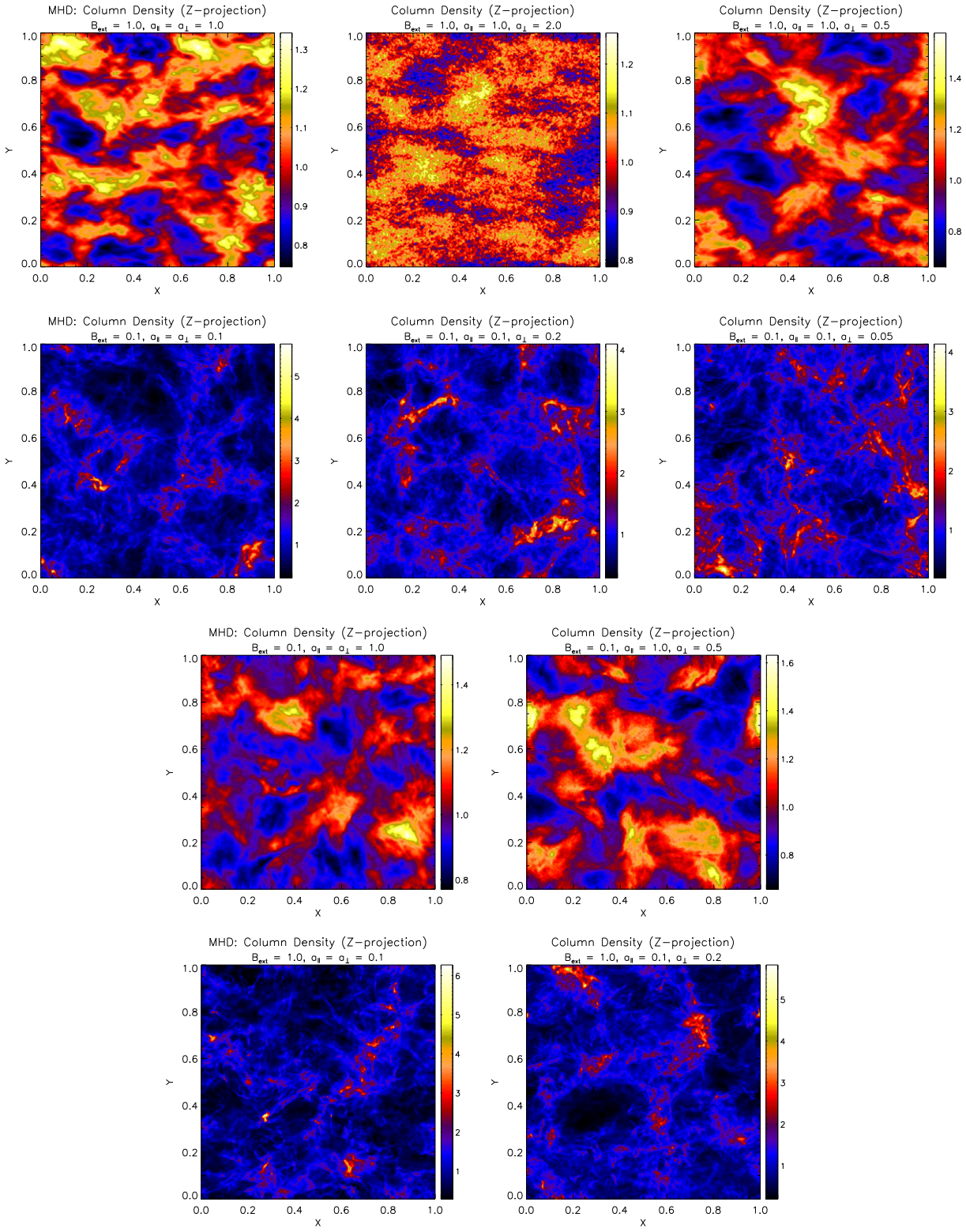

Figure 2. Column density for the different MHD and CGL-MHD models corresponding to the models presented in table 1.

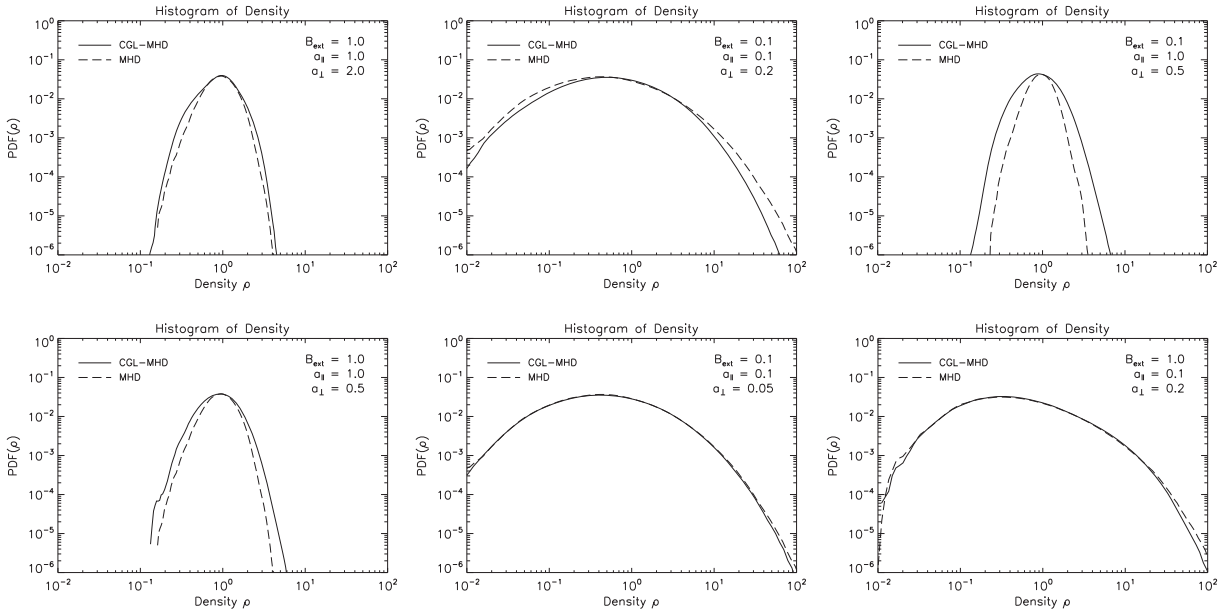

Figure 3. PDFs of density for the studied models. The left column shows models 1 and 2, the middle one shows models 3 and 4, and the right one shows models 4 and 5, according to table 1. For each case, both the CGL-MHD (solid lines) and MHD (dashed lines) models are shown for comparison.

operating that is responsible for changes in the velocity distribution. For model 1 with a weak turbulence, the mirror instability is responsible for the acceleration of the gas resulting in the increase of the *effective* sonic Mach number. In model 6, where initially all cells were stable, the evolution of turbulence causes the instability in most of the computational domain. The instability is responsible here for slowing the gas and reducing the *effective* sonic Mach number.

In figure 3, we present the PDFs of density obtained from each model. In general, the distribution of the gas exhibits an increasing contrast with increasing sonic Mach number. This result is in agreement with the MHD models. However, the kinetic instabilities cause even larger density contrast in the models with weak turbulence, compared to the MHD models. As stated above, in models 1 and 2 the instabilities could freely grow without being suppressed by the turbulent motions of the gas. The PDFs of density for the remaining models show no difference when compared to the MHD models. Surprisingly, in model 5 the firehose instability is responsible for the granulated map of column density, but the PDF of density remains very similar to the MHD case.

The PDFs of velocities are shown in figure 4. Again, the supersonic and super-Alfvenic models (3 and 4) show small differences compared to the standard MHD case. On the other hand, the subsonic and sub-Alfvenic models (1 and 2) present distorted velocity PDFs, with an increase in the high velocity tail. Both instabilities are responsible for more effective acceleration of the plasma, broadening the distribution of velocities. In the case of the firehose instability, the weakly magnetized model presents more evident changes, as noted in model 5. Here, since the magnetic field is weak the perpendicular flows are able to destroy the magnetic field configuration. Therefore, the magnetic breaking is not important, which results in flows with higher velocities. The same process is responsible for the changes in the PDF of

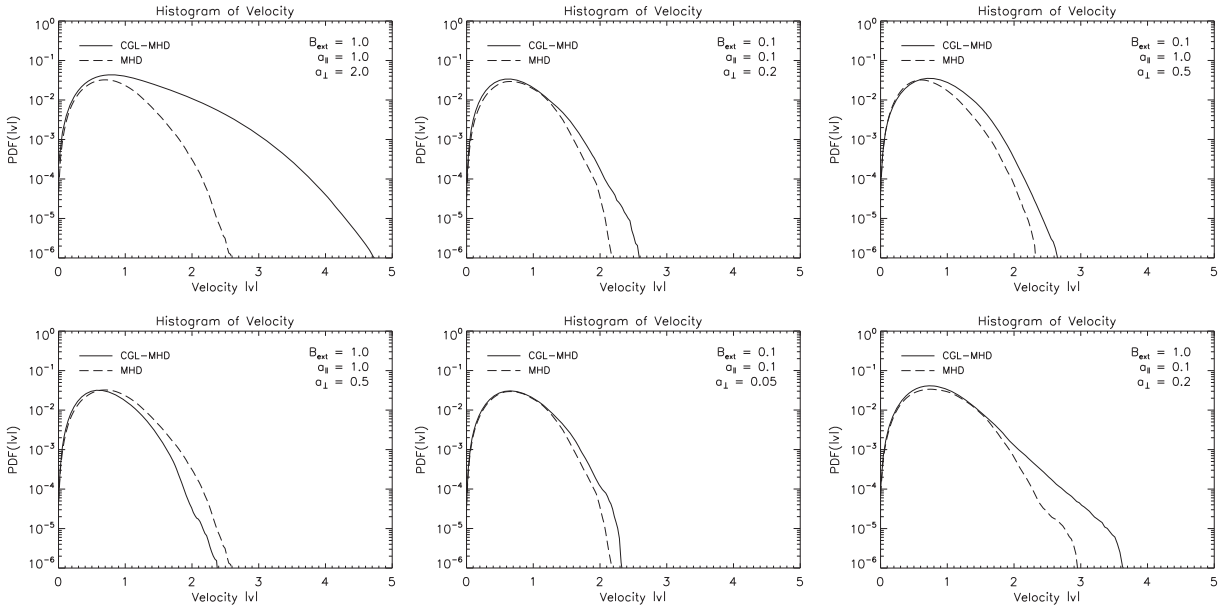

Figure 4. PDFs of velocity for the studied models. The left column shows models 1 and 2, the middle one shows models 3 and 4 and the right one shows models 4 and 5, according to table 1. For each case, both the CGL-MHD (solid lines) and MHD (dashed lines) models are shown for comparison.

model 6. Interestingly, for model 6, we obtained narrower PDF with lower velocities when compared with the MHD case. As the turbulence develops and unstable cells arise, the local magnetic field grows. The strong magnetic breaking takes place, resulting in a low-velocity distribution.

4.2. Power spectra of density and velocity

In order to characterize and study the changes in the energy cascade, as well as the correlations between different scales in CGL-MHD models, we analyze the power spectra. In figures 5 and 6, we present the spectra of fluctuations of density and velocity for all models. Within each plot, we also present the anisotropy of the spectra for parallel and perpendicular directions with respect to the global magnetic field.

In the middle row, we show the plots for models 3 and 4. As also shown previously, there is no substantial difference between the CGL-MHD and the MHD simulations. The density spectra present a similar slope ($\alpha \sim -0.5$) at the inertial range, while a slope of ~ -2 is obtained for the velocity spectra. Regarding the anisotropy ($l_{\parallel} \propto l_{\perp}^{\zeta}$), we found the typical relations $\zeta \sim 1$ at small scales, but the Goldreich and Sidhar (1995) slope $\zeta \sim 2/3$ at larger scales, for both MHD and CGL-MHD simulations. A similar result in the spectra and anisotropy of density was obtained for model 6, with the exception of a slight increase in the spectrum at small scales.

Clearly, there are differences between the spectra of the MHD and CGL-MHD simulations in models 1, 2 and 5. In these cases, the power excess at large values of k because of the fast growth of instabilities in these scales is noticeable. The slopes of the velocity and density spectra

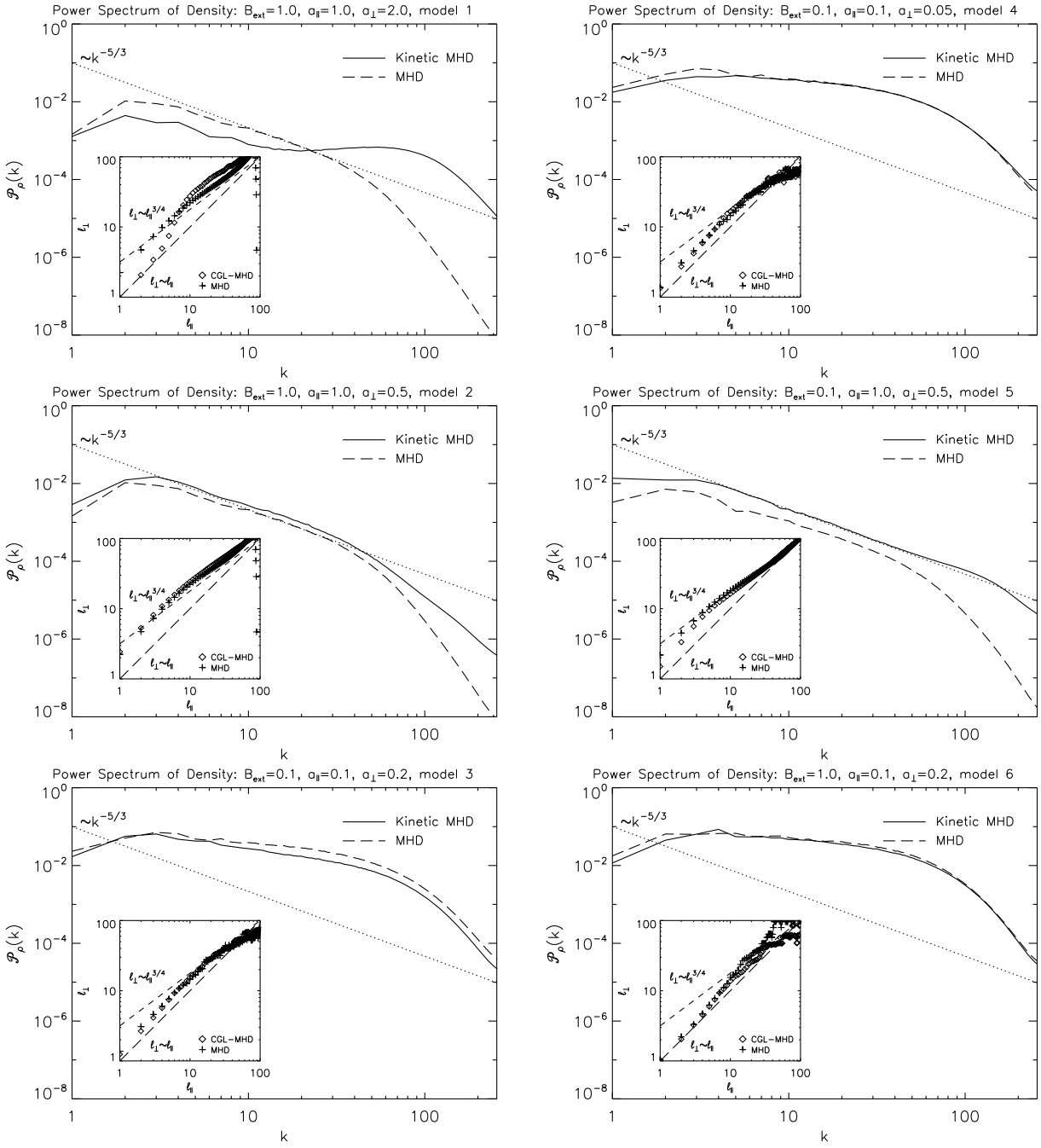

Figure 5. Spectra of density for the studied models, with models 1–3 in the left column and models 4–6 in the right column, according to table 1. For each case, both the MHD (solid lines) and CGL-MHD (dashed lines) models are shown for comparison.

for the MHD models are in the range between -1.7 and -2.0 at the inertial range, whereas CGL-MHD simulations show positive slopes ($\sim +1$ for models 1 and 5) in the velocity spectra and flat density spectra ($\alpha \sim 0$). Regarding the spectral anisotropy, as an interesting result, we

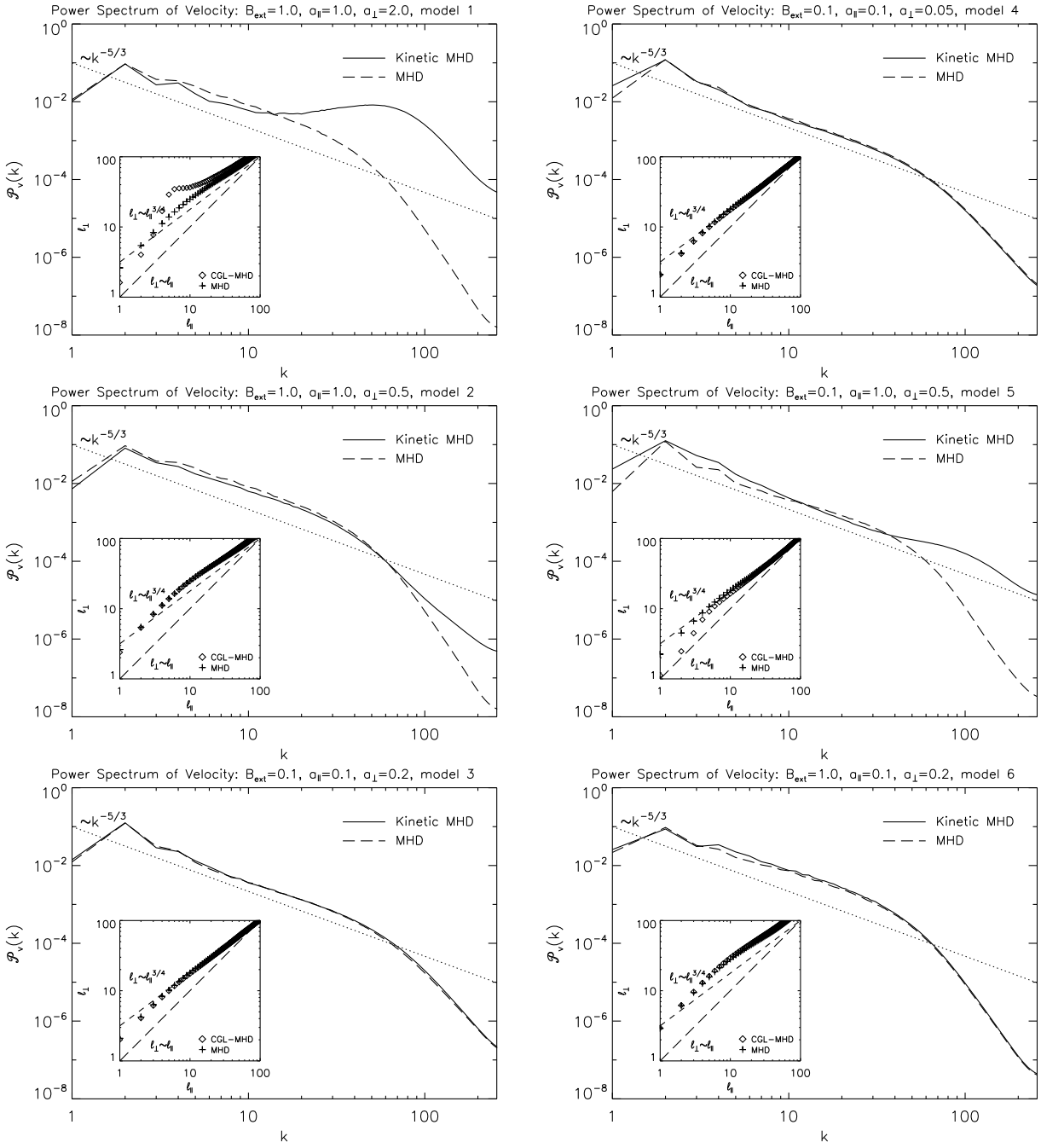

Figure 6. Spectra of velocity for the studied models, with models 1–3 in the left column and models 4–6 in the right column, according to table 1. For each case, both the MHD (solid lines) and CGL-MHD (dashed lines) models are shown for comparison.

see that the firehose instability reduces the anisotropies regarding the global magnetic field lines. A more detailed study of the anisotropy of density and velocity perturbations regarding the local magnetic field is given below.

4.3. Structure functions

In the previous section we showed, from power spectra of density and velocity fluctuation, that the instabilities in CGL-MHD models efficiently transport power from large to small scales, where their concentration is increased. Interesting modifications from MHD turbulence were also shown from the spectral anisotropy regarding the global magnetic field. However, since the instabilities are dominant at small scales, mapping the structure functions regarding the local magnetic field seems to be a better approach if we want to determine the role of instabilities in the isotropization of fluctuations.

The second-order structure function of a given parameter f is defined as

$$\mathrm{SF}(l) = \left\langle |f\,(\mathbf{r}+\mathbf{l}) - f\,(\mathbf{r})|^2 \right\rangle, \tag{6}$$

where $\mathbf{r}$ is the referenced position and $\mathbf{l}$ is the distance calculated along the magnetic field line. The SF is calculated by randomly choosing a large number of referenced positions for each studied correlation length l. Here, to account for the importance of magnetic field fluctuations at small scales, we calculate the correlation length l along the field lines, i.e. in the magnetic field reference frame.

The obtained SFs for density and velocity fluctuations are shown in figures 7 and 8, respectively. In all plots, the solid lines represent the results obtained from the MHD simulations, whereas the dashed lines were obtained from the CGL-MHD simulations. The numbers refer to each model, as described in table 1.

Similar to the previous calculations, model 3 shows no difference between the two theoretical approaches, independent of the scale. The same result is obtained for model 6, which also showed similar spectra for the CGL-MHD and MHD models. Surprisingly, the structure functions of model 4, which showed no differences in PDF and spectra, present more isotropic maps in the CGL-MHD model. The same behavior is obtained for models 2 and 5. These are the models presenting $p_\parallel/p_\perp = 2$, i.e. the firehose instability. Here, the firehose instability is responsible for the generation of small-scale magnetic field fluctuations, tangling the field lines, resulting in an increase of the perpendicular pressure in the local reference frame. Obviously, this effect is overestimated in these calculations because of the double-isothermal approximation. Otherwise, the magnetic field small-scale structure would not change drastically, but the interchange of energy would cause a reduction of parallel pressure anyway. In this sense, the result would be the same, i.e. the firehose instability is responsible for an isotropization of the fluctuations with respect to the magnetic field lines. Model 1, on the other hand, presented a larger anisotropy for the CGL-MHD model. Here, as $p_\parallel/p_\perp = 0.5$, the free energy is mostly converted to kinetic pressure. The mirror instability is responsible for an increase in acceleration of the plasma along the field lines (as already seen in the PDF of velocity), thereby increasing the anisotropy of the fluctuations. The result is more elongated structures, mostly at small and intermediate scales, as also noticed in the power spectra.

5. Discussion

5.1. Time evolution of unstable systems

In order to understand the evolution of the system during the growth and saturation of the instabilities, we calculated the instability condition for the Alfvén and the compressible modes

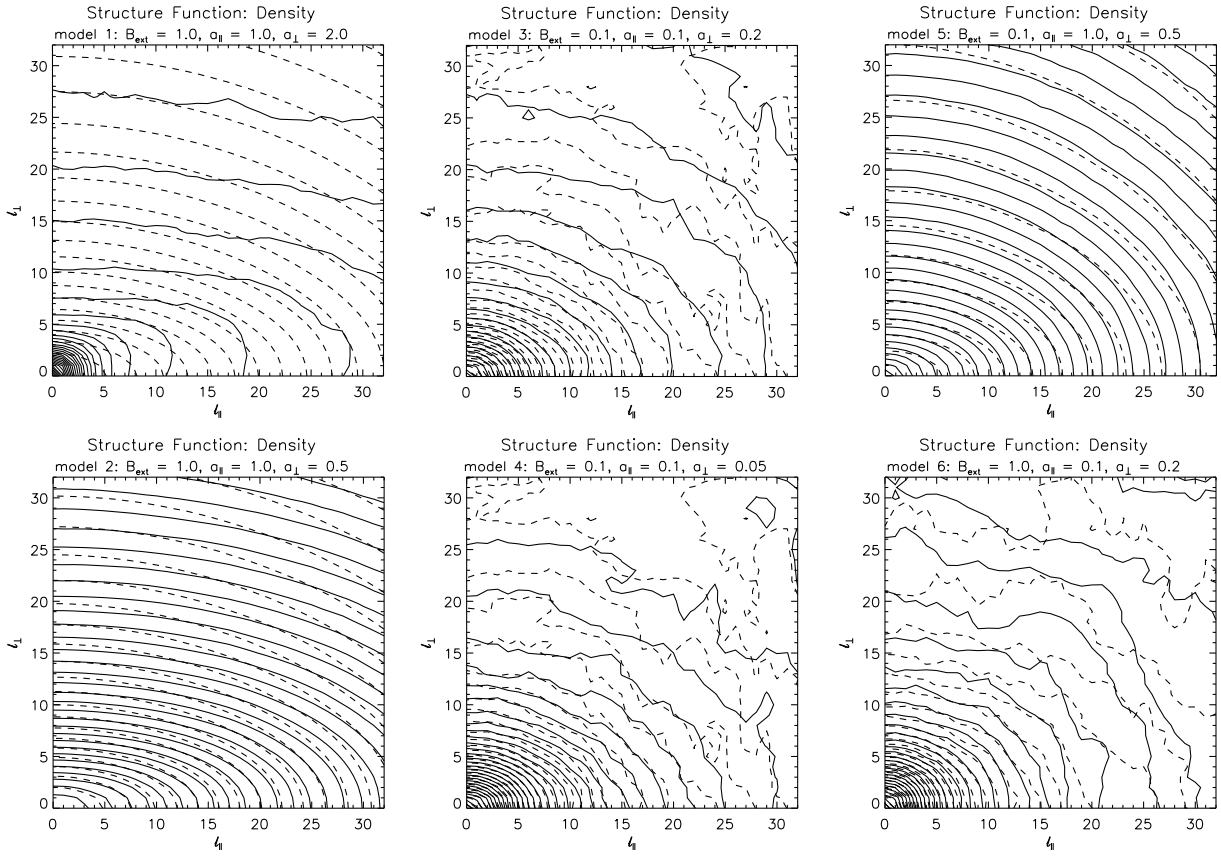

Figure 7. Structure functions of the density in the local reference frame for the studied models. In the left column we show models 1 and 2, in the middle column models 2 and 3 and in the right column models 5 and 6, according to table 1. For each case, both the CGL-MHD (solid lines) and MHD (dashed lines) models are shown for comparison.

for each cell of the computational domain. The dispersion relation of these modes reveal the cells where the instability condition is fulfilled.

As a general behavior, we found that the turbulence increases the range of unstable cells, even for the case with initially stable cells (model 6). This process is illustrated in figure 9 where we show the time evolution of the dispersion relation of model 4 (similar distributions were obtained for all models). Here, we plot the histograms of the stability condition for different times. The Alfvén and magnetosonic modes are independently shown in the left and right plots, respectively. Unstable cells populate the negative range of the dispersion relation. The time is shown in units of the dynamical timescale $\tau_d \sim \delta V/L$.

As the turbulence is injected in the simulation domain, fluctuations of density and magnetic field change the local characteristic speeds and, as a consequence, the stability conditions. This process is fast compared to the dynamical timescale of the system ($t < 0.5\tau_d$). As a result, the dispersion relation is spread over a larger range including the negative values of $(\omega/k)^2$. Then, the instabilities start to grow and saturate, at different timescales for different scales. The saturation of the instability brings the cells towards positive values of $(\omega/k)^2$. At $t \sim 2.5$, most of the cells have already reached the saturation condition for both modes. We believe that

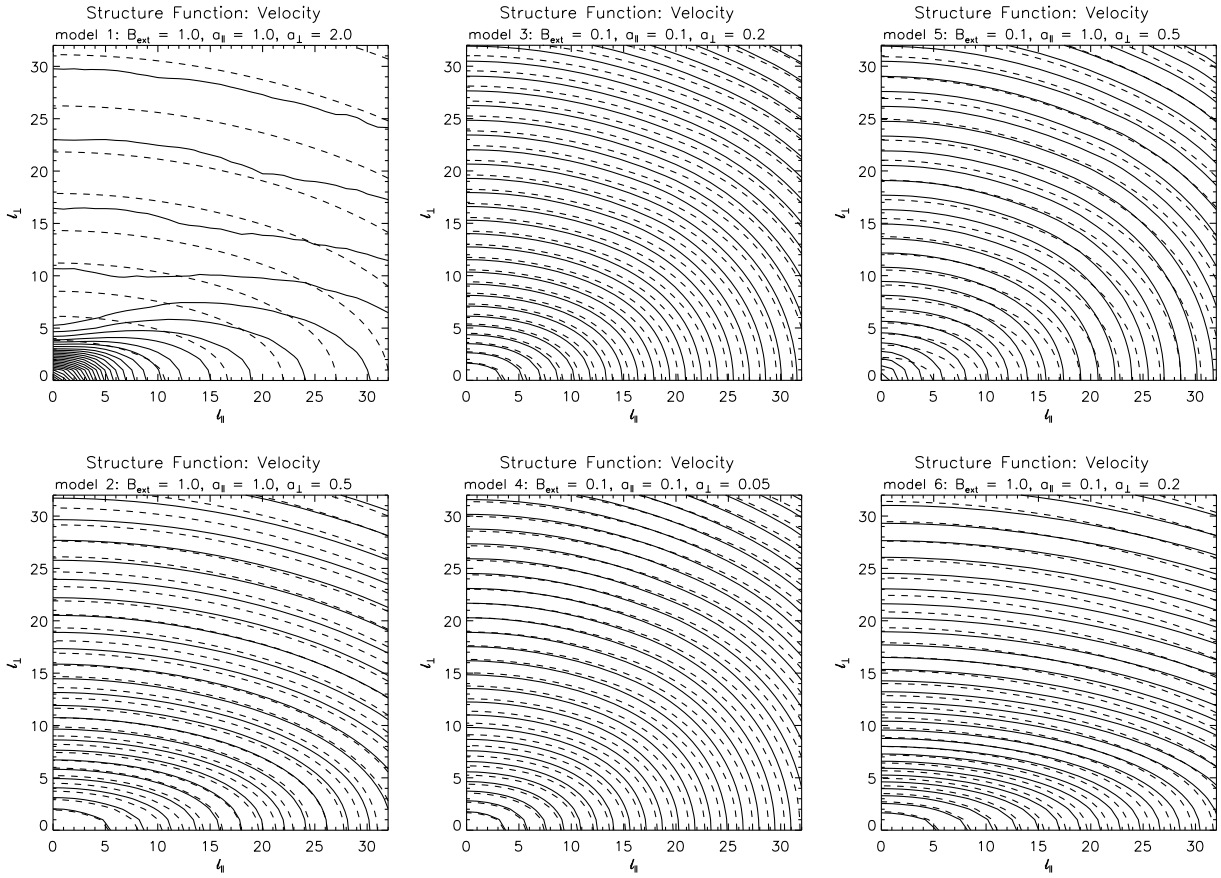

Figure 8. Structure functions of velocity in the local reference frame for the studied models. In the left column we show models 1 and 2, in the middle column models 2 and 3 and in the right column models 5 and 6, according to table 1. For each case, both the CGL-MHD (solid lines) and MHD (dashed lines) models are shown for comparison.

the few still unstable conditions are related to the large-scale fluctuations, which evolve slowly and have higher saturation values. It also seems that the firehose instability of Alfvén modes saturates faster than the magnetosonic mode, although the differences between the modes could be also related to the driving mechanism. We plan to address this possibility in future work.

In the present calculations, we did not perform any wave mode decomposition and therefore we were unable to analyze the time evolution of the individual modes. Also, for this reason we are unable to characterize the time evolution for each wavelength (scale). Needless to say, this is an interesting subject for future studies on CGL-MHD turbulence.

5.2. Changing the pressure anistropy in time

A basic assumption in the double-isothermal closure is that the anisotropy of pressure is kept constant during the whole simulation. The main results of this model are the fast growth and saturation of instabilities that act to reduce the pressure anisotropy. This has not been taken into account in the present work. Would the results remain if the pressure anisotropy changed

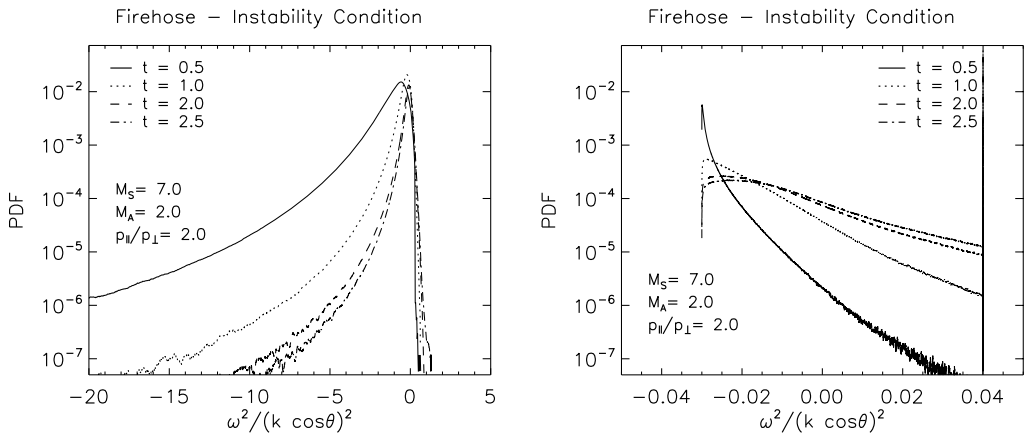

Figure 9. PDF of the stability condition for incompressible Alfvenic (left) and the slow magnetosonic (right) waves.

in time? In order to answer this question, we performed a simulation in which the pressure anisotropy varies in time following a given decay function. The model has been calculated with a numerical resolution of 256^3. Initially, we set the parallel and perpendicular sound speeds to 1.0 and 3.0, respectively, and kept them constant until $t = 2.0$, when the turbulence may be considered as fully developed. From $t = 2.0$, we initiate the decrease of pressure anisotropy by changing the perpendicular sound speed according to $a_\perp(t) = a_{0\perp} + (a_{0\perp} - a_{\infty\perp})/(1 - t_{\rm half}/t)$, where $a_{0\parallel} = 1.0$ and $a_{0\perp} = 3.0$ are the initial values of the sound speed, $a_{\infty\perp} = 1.5$ is the perpendicular sound speed in the limit $t \to \infty$, and $t_{\rm half} = 1.0$ is the time after which the perpendicular speed decays to the value of $(a_{0\perp} + a_{\infty\perp})/2$. The parallel sound speed is also changed, so $a_\parallel^2(t) + 2a_\perp^2(t)$ is kept constant and equal to the initial value, i.e. the total pressure is kept constant and there is an interplay between the parallel and perpendicular ones. In this way, we change the pressure anisotropy in time starting from the unstable regime and ending up in the stable regime.

In figure 10, we show the evolution of the velocity field anisotropy, taken from the structure function calculated for a given separation length $l_\parallel = 10$ (symbols). The change in the sound speed ratio $a_\parallel/a_\perp$ is plotted as well (solid line). It is clear that the anisotropy of velocity fluctuations oscillates around the constant value 3.4, while the double-isothermal closure is assumed. At $t = 2.0$, the sound speed ratio increases following the adopted function, resulting in a simultaneous increase in $l_\parallel/l_\perp$, i.e. a decrease in the anisotropy of the velocity fluctuations. At $t \approx 2.6$ the system enters the stable regime (crossing the MHD regime), where the collisionless plasma instabilities are not relevant. Therefore, with decreasing the pressure anisotropy even further, the velocity fluctuations retain their anisotropy.

This result is particularly important, as it demonstrates that the anisotropy of velocity fluctuations is not related to any numerical dissipation at small scales, but rather due to the presence of physical instabilities. On the other hand, this result also reveals that the system evolves fast enough to change its velocity distribution to the saturation regime (crossing the MHD regime) once the pressure anisotropy is reduced. In other words, turbulent motions in the post-anisotropic pressure phase wash out all of the peculiar features in the statistics of velocity observed during the anisotropic phase. Therefore, is collisionless plasma turbulence unable to *remember* its unstable phase?

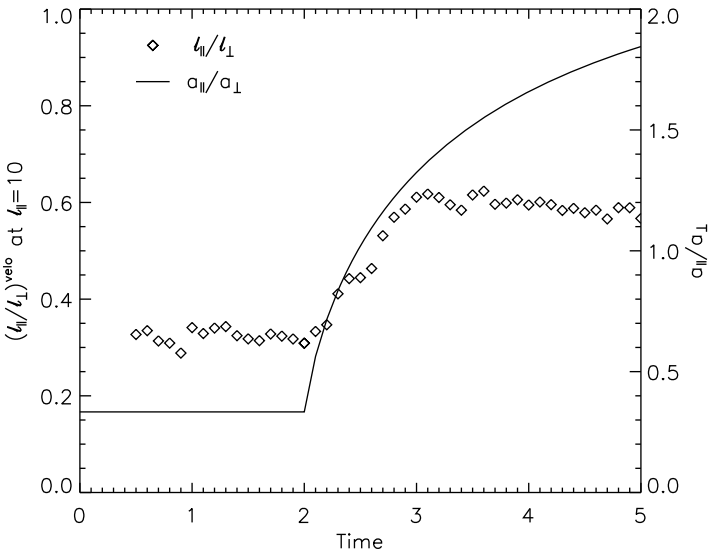

Figure 10. Time evolution of the anisotropy of velocity fluctuations $(l_\parallel/l_\perp)$ obtained for the separation length $l_\parallel = 10$ (symbols) and of the sound speed ratio $a_\parallel/a_\perp$ (solid line).

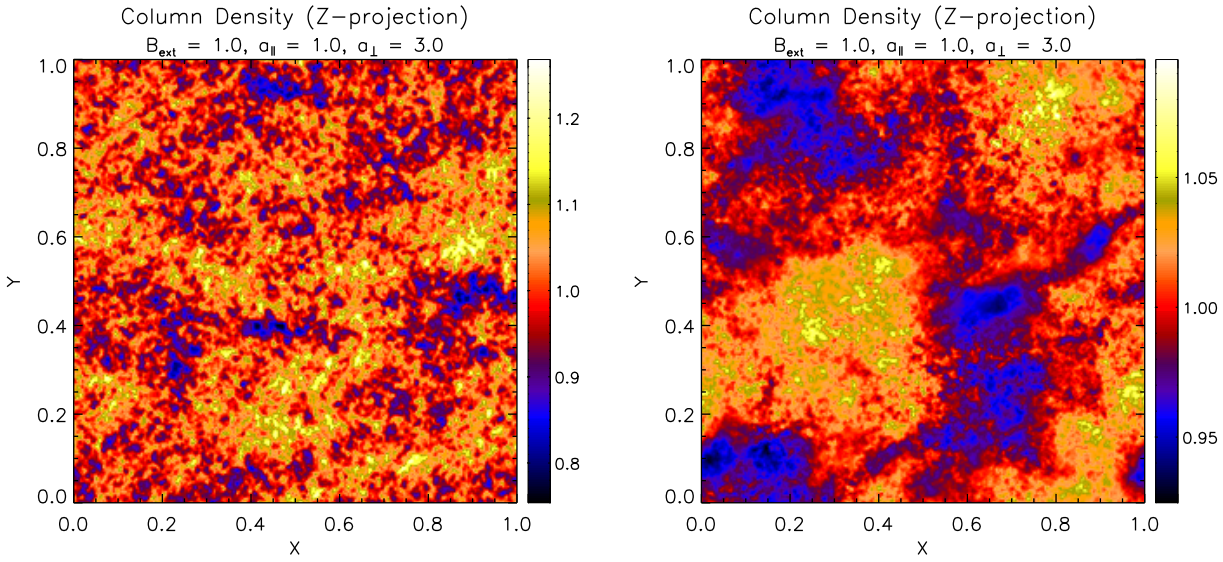

Figure 11. Column density maps for $t = 2$ (left) and $t = 5$ (right).

It is well known, from MHD cases, that the inertia of the high-density regions to the turbulent motions is large. This indicates that the density distribution should preserve its features, related to the past unstable phases, longer than the corresponding features of the velocity field distribution. This is indeed observed in this test simulation of decreasing pressure anisotropy. In figure 11, we show the column density maps calculated for $t = 2$ (left) and $t = 5$ (right). At $t = 2.0$, the instabilities are responsible for the large power at small scales. The relative power of the small scales decreases with the pressure anisotropy, as seen for $t = 5.0$, while large scales clearly appear that may be directly compared to

the MHD case shown in figure 2. However, as compared to the MHD case in figure 2, the power at small scales is much larger; that is, even though the pressure anisotropy is reduced and turbulent motions become more or less similar to the MHD case, the density distribution still reveals large fluctuations at small scales created during the unstable phase. This is of great importance from the observational point of view, since observers could search for past unstable phases in clusters of galaxies from the column density distributions of the ICM plasma.

5.3. Applicability of the double-isothermal case

The basic assumption in the double-isothermal closure is that the anisotropy of pressures is kept constant during the entire simulation. In a more realistic scenario, two main mechanisms, the anisotropic radiative losses and the instabilities mentioned in this work, would break the double-isothermal condition. What is the application of the double-isothermal closure then?

Needless to say, the physical study of this special case is important to provide a crude but simpler estimation of the evolution of instabilities in turbulent collisionless plasmas. In a realistic situation, however, the typical physical timescales will determine the evolution of the system. The anisotropic radiative losses, such as cyclotron emission, determine the radiative isotropization timescale $\tau_{\rm rad}$. The instabilities, e.g. firehose and mirror, determine the timescale $\tau_{\rm ins}$. If $\tau_{\rm rad} \ll \tau_{\rm ins}$, the radiative losses would be dominant and the effects of instabilities on the statistics of turbulence would be negligible. This case is of no interest for this work. If $\tau_{\rm rad} \gg \tau_{\rm ins}$, double-adiabatic closure should be used. Actually, both timescales depend on the physical length scale and the two regimes could be found in the same system, being $\tau_{\rm rad} \ll \tau_{\rm ins}$ at large scales and $\tau_{\rm rad} \gg \tau_{\rm ins}$ at small scales. However, what are the sources of pressure anisotropy? One of the possible mechanisms is turbulence itself. Even though injection of turbulent motions is isotropic, which is probably not true, the developing magnetized turbulence is not. The parallel, with respect to magnetic field lines, amplitude of the turbulent motions is larger than the perpendicular. This results typically in a firehose instability condition. If injection of kinetic energy is continuous, $\tau_{\rm inj} \ll \tau_{\rm ins}$ and $\tau_{\rm inj} \ll \tau_{\rm rad}$, resulting in an almost 'constant' pressure anisotropy.

Random galactic motions and the central engine, the active galactic nucleus (AGN), are the main sources of kinetic energy of the ICM plasma. These continuous sources of turbulence may be considered as the main reason for an eventual pressure anisotropy observed in the ICM. In this case, the double-isothermal closure is applicable.

6. Conclusions

In this work, we have presented the first extensive statistical analysis of 3D simulations of turbulence in collisionless plasma. We studied the case of double-isothermal closure of the CGL-MHD equations in order to compare our results with previous isothermal simulations of MHD turbulence. We performed simulations with different characteristic sonic and Alfvenic Mach numbers, as well as different pressure anisotropies to account for both firehose and mirror instabilities. As the main results, we showed that:

- we obtained firehose/mirror unstable conditions in all simulations. The unstable conditions may be created, even for stable initial conditions, as a consequence of the driving and evolutions of the turbulent cascade;

- the supersonic and super-Alfvenic models showed no significant differences when compared with standard MHD models. Basically, strong turbulence is able to destroy the changes in the small-scale structure resulting from the instabilities;
- the PDFs of density showed broadened profiles for the subsonic and sub-Alfvenic cases. The PDFs of velocity showed changes for sub-Alfvenic models. Specifically, we obtained an increase in the number high-velocity flows in subsonic models, and its decrease for supersonic turbulence;
- the spectra of density and velocity showed an increase in power at small scales for subsonic models;
- the structure functions of velocity and density fluctuations revealed that the firehose instability tends to isotropize the fluctuations regarding the local reference frame, i.e. along the magnetic field lines. On the other hand, the mirror instability increases the elongation of fluctuations along the magnetic field lines;
- the dynamical timescale ($\tau_d \sim \delta V/L$) may also be a good estimate for the saturation timescale of the instability growth of most of the wavelengths. This fast evolution of the system implies interesting physical processes; for example, interchange of energy and acceleration of cosmic rays in the collisionless plasma at ICM of galaxies. The growth rate of long wavelengths may be much larger than τ_d.

Acknowledgments

GK, DFG and AL acknowledge financial support from the NSF (no. AST0307869), the Center for Magnetic Self-Organization in Astrophysical and Laboratory Plasmas and the Brazilian agencies FAPESP (no. 06/57824-1 and 07/50065-0) and CAPES (no. 4141067).

Appendix. Linearization of the double-isothermal CGL-MHD equations

In this appendix, we derive the dispersion relation for the double-isothermal CGL-MHD equations. We start from the isotropic case $a_\parallel^2 = a_\perp^2$, since it is the case of ideal MHD, and then extend the analysis including the anisotropy term by introducing the pressure tensor. In this way, we can identify the role of the anisotropy pressure directly.

The ideal double-isothermal CGL-MHD equations with the pressure isotropy assumption $p_\parallel \equiv a_\parallel^2 \rho = p_\perp \equiv a_\perp^2 \rho$ result in $\mathsf{P} = a_\perp^2 \rho I$ and can be written in non-conservative form as follows,

$$\frac{\partial \rho}{\partial t} + \boldsymbol{v} \cdot \nabla \rho + \rho \nabla \cdot \boldsymbol{v} = 0, \tag{A.1}$$

$$\rho \frac{\partial \boldsymbol{v}}{\partial t} + \rho \boldsymbol{v} \cdot \nabla \boldsymbol{v} + a_\perp^2 \nabla \rho - \frac{1}{4\pi} (\nabla \times \boldsymbol{B}) \times \boldsymbol{B} = 0, \tag{A.2}$$

$$\frac{\partial \boldsymbol{B}}{\partial t} - \nabla \times (\boldsymbol{v} \times \boldsymbol{B}) = 0, \tag{A.3}$$

where ρ is the density, $\boldsymbol{v}$ is the velocity field, $\boldsymbol{B}$ is the magnetic field, and $a_\perp$ and $a_\parallel$ are the sound speeds in the perpendicular and parallel directions with respect to $\boldsymbol{B}$, respectively.

We assume that all variables can be separated into the uniform and fluctuating components, i.e. $\rho \to \rho_0 + \delta\rho$, $\boldsymbol{v} \to \boldsymbol{v}_0 + \delta\boldsymbol{v}$, $\boldsymbol{B} \to \boldsymbol{B}_0 + \delta\boldsymbol{B}$. We also assume the lack of uniform flow,

i.e. $\boldsymbol{v}_0 = 0$. Substituting the variable separation in equations (A.1)–(A.3) and removing all nonlinear terms leads to the following set of equations,

$$\frac{\partial \delta\rho}{\partial t} + \rho_0 \nabla \cdot \delta\boldsymbol{v} = 0, \tag{A.4}$$

$$\rho_0 \frac{\partial \delta\boldsymbol{v}}{\partial t} + a_\perp^2 \nabla\delta\rho - \frac{1}{4\pi}(\nabla \times \delta\boldsymbol{B}) \times \boldsymbol{B}_0 = 0, \tag{A.5}$$

$$\frac{\partial \delta\boldsymbol{B}}{\partial t} - \nabla \times (\delta\boldsymbol{v} \times \boldsymbol{B}_0) = 0. \tag{A.6}$$

Introducing the variable perturbation of the form $\delta f(\mathbf{x}, t) \propto \exp[\mathbf{i}(\mathbf{k}\cdot\mathbf{x} - \omega t)]$ results in the above set of equations represented in the Fourier space,

$$-\omega\delta\rho + \rho_0 (\boldsymbol{k} \cdot \delta\boldsymbol{v}) = 0, \tag{A.7}$$

$$-\omega\rho_0\delta\boldsymbol{v} + a_\perp^2 \delta\rho\boldsymbol{k} - \frac{1}{4\pi}(\boldsymbol{k} \times \delta\boldsymbol{B}) \times \boldsymbol{B}_0 = 0, \tag{A.8}$$

$$-\omega\delta\boldsymbol{B} - \boldsymbol{k} \times (\delta\boldsymbol{v} \times \boldsymbol{B}_0) = 0. \tag{A.9}$$

Multiplying equation (A.8) by ω, dividing by ρ_0 and substituting equations (A.7) and (A.9), we obtain the dispersion relation,

$$-\omega^2\delta\boldsymbol{v} + a_\perp^2 (\boldsymbol{k}\cdot\delta\boldsymbol{v})\,\boldsymbol{k} + \frac{1}{4\pi\rho_0}\{[\boldsymbol{k}(\boldsymbol{B}_0\cdot\boldsymbol{B}_0) - \boldsymbol{B}_0(\boldsymbol{B}_0\cdot\boldsymbol{k})](\boldsymbol{k}\cdot\delta\boldsymbol{v}) - \boldsymbol{k}(\boldsymbol{k}\cdot\boldsymbol{B}_0)(\boldsymbol{B}_0\cdot\delta\boldsymbol{v}) + (\boldsymbol{k}\cdot\boldsymbol{B}_0)(\boldsymbol{B}_0\cdot\boldsymbol{k})\,\delta\boldsymbol{v}\} = 0. \tag{A.10}$$

Without losing generality, we can assume that the mean magnetic field is parallel to the X-direction, i.e. $\boldsymbol{B}_0 = B_0\hat{x}$, and $\boldsymbol{k}$ lies in the XY-plane under an angle θ with the respect to $\boldsymbol{B}_0$, i.e. $\boldsymbol{k} = k(\cos\theta\hat{x} + \sin\theta\hat{y})$. We also introduce the Alfvén speed $c_\mathrm{A} \equiv B_0/\sqrt{4\pi\rho_0}$. Substituting these assumptions and dividing the dispersion relation by k^2, we can express it in matrix form,

$$\mathsf{A}\,\delta\boldsymbol{v} = \begin{pmatrix} -\frac{\omega^2}{k^2} + a_\perp^2\cos^2\theta & a_\perp^2\sin\theta\cos\theta & 0 \\ a_\perp^2\sin\theta\cos\theta & -\frac{\omega^2}{k^2} + a_\perp^2\sin^2\theta + c_\mathrm{A}^2 & 0 \\ 0 & 0 & -\frac{\omega^2}{k^2} + c_\mathrm{A}^2\cos^2\theta \end{pmatrix} \begin{pmatrix} \delta v_x \\ \delta v_y \\ \delta v_z \end{pmatrix} = 0. \tag{A.11}$$

The determinant of the matrix A gives the dispersion relation,

$$\det\mathsf{A} = \left(-\frac{\omega^2}{k^2} + c_\mathrm{A}^2\cos^2\theta\right)\left[\frac{\omega^4}{k^4} - \frac{\omega^2}{k^2}(a_\perp^2 + c_A^2) + c_\mathrm{A}^2 a_\perp^2\cos^2\theta\right] = 0, \tag{A.12}$$

with the eigenvalues

$$\left(\frac{\omega^2}{k^2}\right)_\mathrm{A} = c_\mathrm{A}^2\cos^2\theta \tag{A.13}$$

corresponding to the Alfvén wave and

$$\left(\frac{\omega^2}{k^2}\right)_{f,s} = \frac{1}{2}\left[a_\perp^2 + c_\mathrm{A}^2 \pm \sqrt{\left(a_\perp^2 + c_\mathrm{A}^2\right)^2 - 4a_\perp^2 c_\mathrm{A}^2\cos^2\theta}\right] \tag{A.14}$$

corresponding to the fast and slow magnetosonic waves, respectively.

In the next step, we include the pressure anisotropy term in the motion equation (A.2), which for the double-isothermal approximation can be written as

$$\nabla\cdot[(p_\parallel-p_\perp)\hat{b}\hat{b}] = (a_\parallel^2-a_\perp^2)\nabla\cdot(\rho\hat{b}\hat{b})$$
$$= (a_\parallel^2-a_\perp^2)\left\{\hat{b}(\hat{b}\cdot\nabla)\rho+\frac{\rho}{B}(\hat{b}\cdot\nabla)\boldsymbol{B}-\frac{2\rho}{B}[(\hat{b}\cdot\nabla\boldsymbol{B})\cdot\hat{b}]\hat{b}\right\}. \tag{A.15}$$

Substituting the variables separation in this term, we obtain

$$\nabla\cdot\delta[(p_\parallel-p_\perp)\hat{b}\hat{b}] = (a_\parallel^2-a_\perp^2)$$
$$\times\left\{\hat{b}_0(\hat{b}_0\cdot\nabla)\delta\rho+\frac{\rho_0}{B_0}(\hat{b}_0\cdot\nabla)\delta\boldsymbol{B}-\frac{2\rho_0}{B_0}[(\hat{b}_0\cdot\nabla\delta\boldsymbol{B})\cdot\hat{b}_0]\hat{b}_0\right\}, \tag{A.16}$$

where $\hat{b}_0\equiv\boldsymbol{B}_0/B_0$, and the first term corresponds to the perturbation of the density, and two remaining terms correspond to the perturbation of magnetic field. Introducing the perturbed variables of the form as before, i.e. $\delta f(\mathbf{x},\mathbf{t})\propto\exp[\mathbf{i}(\mathbf{k}\cdot\mathbf{x}-\omega\mathbf{t})]$, the term (A.16) can be written in Fourier space as

$$\boldsymbol{k}\cdot\delta[(p_\parallel-p_\perp)\hat{b}\hat{b}] = (a_\parallel^2-a_\perp^2)(\hat{b}_0\cdot\boldsymbol{k})\left\{\hat{b}_0\delta\rho+\frac{\rho_0}{B_0}\delta\boldsymbol{B}-\frac{2\rho_0}{B_0}(\hat{b}_0\cdot\delta\boldsymbol{B})\hat{b}_0\right\}. \tag{A.17}$$

Next, we multiply it by ω and substitute equations (A.4) and (A.6) to obtain the simpler relation

$$\omega\boldsymbol{k}\cdot\delta[(p_\parallel-p_\perp)\hat{b}\hat{b}] = \rho_0(a_\parallel^2-a_\perp^2)(\boldsymbol{k}\cdot\hat{b}_0)^2[2\hat{b}_0(\hat{b}_0\cdot\delta\boldsymbol{v})-\delta\boldsymbol{v}]. \tag{A.18}$$

Finally, assuming $\boldsymbol{B}_0=B_0\hat{x}$ and $\boldsymbol{k}=k(\cos\theta\hat{x}+\sin\theta\hat{y})$, the term reduces to a very simple expression,

$$\frac{\omega}{k^2}\frac{1}{\rho_0}\boldsymbol{k}\cdot\delta[(p_\parallel-p_\perp)\hat{b}\hat{b}] = (2\delta v_x\hat{b}_0-\delta\boldsymbol{v})(a_\parallel^2-a_\perp^2)\cos^2\theta. \tag{A.19}$$

Rewriting this term in matrix form, we obtain the contribution to the matrix A resulting from the presence of pressure anisotropy,

$$\Delta\mathsf{A}\,\delta\boldsymbol{v} = \begin{pmatrix}(a_\parallel^2-a_\perp^2)\cos^2\theta & 0 & 0\\ 0 & -(a_\parallel^2-a_\perp^2)\cos^2\theta & 0\\ 0 & 0 & -(a_\parallel^2-a_\perp^2)\cos^2\theta\end{pmatrix}\begin{pmatrix}\delta v_x\\ \delta v_y\\ \delta v_z\end{pmatrix}. \tag{A.20}$$

The matrix $\mathsf{A}+\Delta\mathsf{A}$ takes form

$$\begin{pmatrix}-\frac{\omega^2}{k^2}+a_\parallel^2\cos^2\theta & a_\perp^2\sin\theta\cos\theta & 0\\ a_\perp^2\sin\theta\cos\theta & -\frac{\omega^2}{k^2}+c_A^2+a_\perp^2-a_\parallel^2\cos^2\theta & 0\\ 0 & 0 & -\frac{\omega^2}{k^2}+[c_A^2-(a_\parallel^2-a_\perp^2)]\cos^2\theta\end{pmatrix}, \tag{A.21}$$

and its determinant gives the dispersion relation for the CGL-MHD equations,

$$\det\mathsf{A} = \left\{-\frac{\omega^2}{k^2}+[c_A^2-(a_\parallel^2-a_\perp^2)]\cos^2\theta\right\}$$
$$\times\left\{\frac{\omega^4}{k^4}-\frac{\omega^2}{k^2}(c_A^2+a_\perp^2)+[a_\parallel^2(c_A^2+a_\perp^2-a_\parallel^2\cos^2\theta)-a_\perp^4\sin^2\theta]\cos^2\theta\right\}=0, \tag{A.22}$$

with the eigenvalues

$$\left(\frac{\omega^2}{k^2}\right)_A = [c_A^2 - (a_\parallel^2 - a_\perp^2)]\cos^2\theta, \tag{A.23}$$

corresponding to the Alfvén wave and

$$\left(\frac{\omega^2}{k^2}\right)_{f,s} = \frac{1}{2}\left\{b^2 \pm \sqrt{b^4 - 4[a_\parallel^2(b^2 - a_\parallel^2\cos^2\theta) - a_\perp^4\sin^2\theta]\cos^2\theta}\right\}, \tag{A.24}$$

corresponding to the fast and slow magnetosonic waves, respectively, where $b^2 \equiv a_\perp^2 + c_A^2$. The derived dispersion relations determine the stability conditions for all characteristic waves and growth rates for the firehose and mirror instabilities.

References

Chew G F, Goldberger M L and Low F E 1956 *Proc. R. Soc.* A **236** 12
Einfeldt B, Munz C D, Roe P L and Sjögreen B 1991 *J. Comput. Phys.* **92** 273
Ensslin T A and Vogt C 2006 *Astron. Astrophys. J.* **453** 447
Goldreich P and Sidhar S 1995 *Astrophys. J.* **438** 763
Hasegawa A 1969 *Phys. Fluids* **12** 2642
Hau L-N 2002 *Phys. Plasmas* **9** 2455
Hau L-N and Sonnerup U O 1993 *Geophys. Rev. Lett.* **20** 1763
Hau L-N and Wang B-J 2007 *Nonlinear Process. Geophys.* **14** 557
Howes G G *et al* 2006 *Astrophys. J.* **651** 590
Kowal G, Lazarian A and Beresnyak A 2007 *Astrophys. J.* **658** 423
Kowal G, Lazarian A, Vishniac E T and Otmianowska-Mazur K 2009 *Astrophys. J.* **700** 63
Kowal G and Lazarian A 2010 *Astrophys. J.* **720** 742
Passot T and Sulem P L 2006 *J. Geophys. Res.* **111** 4203
Press W H, Teukolsky S A, Vetterling W T and Flannery B P 1992 *Numerical Recipes in C: the Art of Scientific Computing* 2nd edn (New York: Cambridge University Press)
Quest K B and Shapiro V D 1996 *J. Geophys. Res.* **101** A11 24457
Schekochihin A A *et al* 2005 *Astrophys. J.* **629** 139
Schekochihin A A *et al* 2008 *Phys. Rev. Lett.* **100** 081301
Sharma P, Hammett G W and Quataert E 2003 *Astrophys. J.* **596** 1121
Sharma P, Hammett G W, Quataert E and Stone J M 2006 *Astrophys. J.* **637** 952
Tóth G 2000 *J. Comput. Phys.* **161** 605
Wang B-J and Hau L-N 2003 *J. Geophys. Res.* **108** 1463